Available online at www.sciencedirect.com
ScienceDirect
Journal of Solid State Chemistry 181 (2008) 997–1004
JOURNAL OF SOLID STATE CHEMISTRY
www.elsevier.com/locate/jssc

Electron microscopic studies of the antiferroelectric phase in $Sr_{0.60}Ca_{0.40}TiO_3$ ceramic

Shahid Anwar, N.P. Lalla*

UGC-DAE Consortium for Scientific Research, University Campus, Khandwa Road, Indore 452001, India

Received 28 September 2007; received in revised form 3 December 2007; accepted 4 February 2008
Available online 20 February 2008

Abstract

The structural variants and their coexistence across the antiferroelectric phase transition in $Sr_{0.60}Ca_{0.40}TiO_3$ ceramic has been studied through transmission electron microscopy (TEM) at room temperature and ~100 °C. A clear evidence of the presence of superlattice reflections, corresponding to the cell doubling along the *c*-axis of *Pbnm* (or *b*-axis along *Pnma*), occurring during paraelectric to antiferroelectric transition, has been obtained through selected area electron diffraction, convergent beam electron diffraction and lattice-resolution imaging. Coexistence of the *Pbnm* and *Pbcm* phases at room temperature has been observed and attributed to the strain/disorder-induced broadening of the first-order antiferroelectric phase transition. Drastic changes in the domain structure during *Pbnm* to *Pbcm* transformation have been observed. This clearly indicates that the antiferrodistortive transition responsible for the occurrence of the antiferroelectric phase is of completely different origin and it is not just an additional follow-up of the already-existing ordering due to $a^-a^-c^+$ tilt schemes in the *Pbnm* domain. Thermal cycling studies on microstructural changes indicate some kind of memory mechanism, which retains the memory of the original $a^-a^-c^+$ tilt schemes in the *Pbnm* phase. This has been attributed to the symmetry conforming short-range order (SC-SRO) of the point defects.

Keywords: Electron diffraction; CBED; X-ray diffraction; Antiferroelectric ceramics; SC-SRO

1. Introduction

The apparent simplicity of the perovskite structure belies the difficulties in precisely identifying the structure of many of the distorted perovskites. Therefore the study of the evolution of different crystallographic phases and the corresponding microstructures of perovskites, as a function of temperature, composition and pressure, has always been an area of continued interest. Most of the perovskites under go a variety of structural phase transformations, which involve tilt and distortion of the anion octahedra in various ways [1–3]. Of these, the structure of the $Sr_{1-x}Ca_xTiO_3$ (SCT) perovskite system has been a subject of a number of studies by several groups [4–8]. SCT shows a variety of dielectric and structural properties with changing Ca content. It behaves as a quantum ferroelectric [9], for $0.0018<x<0.016$ and as relaxors for $0.016<x<0.12$ [9,10]. Ranjan et al. [10,11] have observed an antiferroelectric phase in SCT for $0.12<x<0.40$, whose transition temperature increases with increasing Ca content. The observed antiferroelectric phase transition has been attributed to the antiparallel displacement of Sr/Ca and Ti ions, resulting in antiparallel aligned dipoles giving rise to a crystal structure with space-group *Pbcm*. This has been supported by neutron diffraction studies [12,13], which give the evidence of the superlattice peaks corresponding to unit cell doubling along the *c*-axis. For SCT ceramics with Ca composition between $0.35<x<0.41$, the antiferroelectric (*Pbcm*) transition occurs above the room temperature, i.e. for these compositions the antiferroelectric (*Pbcm*) phase will be observed at room temperature itself. The XRD, Raman and neutron-scattering studies are in conformity with this [10–14]. But to the best of our knowledge there is no study that describes the observation of the superlattice ordering using electron diffraction in transmission electron microscope (TEM). Electron diffraction has an advantage over the other techniques that

*Corresponding author. Fax: +91 7312462294.
E-mail address: nplalla@csr.ernet.in (N.P. Lalla).

0022-4596/$ - see front matter © 2008 Elsevier Inc. All rights reserved.
doi:10.1016/j.jssc.2008.02.004

diffraction data from single-crystal domains can be routinely obtained from relatively much smaller regions of $<0.1\,\mu m$, which is not possible by any other technique. Since electrons interact much more strongly with the oxygen sub-lattice than that of the X-rays, electron diffraction allows direct observation of even the weakest superlattice peaks. Moreover since the described antiferroelectric transition is first order [10,15], its width may broaden [16] depending on the amount of intrinsic disorder/strain present in the sample, and may reach much beyond the transition temperature and show phase-coexistence in both super-cooled and super-heated regimes. In the coexisting condition, phases will usually be quite small and may not be unambiguously detected through bulk techniques such as XRD. In such cases confirmatory evidence of the possible phase-coexistence requires microscopic imaging and diffraction investigation, and TEM is the only such tool. Keeping this in view involved TEM investigation has been carried out on SCT40 ceramic at room temperature and 100 °C.

2. Experimental

$Sr_{0.60}Ca_{0.40}TiO_3$ (SCT40) ceramic has been prepared through semi-wet route involving thermochemical reactions. For this the $Sr_{0.60}Ca_{0.40}CO_3$ precursor was synthesized using ammonium carbonate solution as a precipitant in a stoichiometric mixture of $SrNO_3$ and $CaNO_3$ aqueous solutions, as described in detail by Ranjan et al. [13]. The $Sr_{0.60}Ca_{0.40}CO_3$ precursor and TiO_2 powder were preheated at 150 °C to remove moisture and were thoroughly mixed in stoichiometric proportions. Isopropyl alcohol was used as a mixing medium. After several cycles of mixing and drying, the mixture was calcined at 1100 °C and 1250 °C for 12 h each. The calcined powder was reground, mixed with a binder (polyvinyl alcohol) and then pelletized into 15 mm diameter pellets at a uniaxial pressure of 100 kN/cm^2. The pellets were then sintered at 1300 °C for 12 h. The sintered pellets were gently crushed to fine powder and subsequently annealed at 600 °C for ~10 h to remove the residual strains that might appear during grinding of the sintered pellet. The strain-free powder was then subjected to X-ray diffraction (XRD) for phase purity and structural characterizations. The TEM sample was prepared by cutting a 3 mm disk from the pellet. The disk was mechanically thinned to ~70 μm and then subsequently dimpled to ~35 μm. The dimpled disk was then made electron transparent by ion-beam polishing employing twin argon ion guns set at a grazing incidence of 3° and operating at 3.3 kV. TEM was carried out employing Tecnai G^{2}20 TEM (FEI) operating at 200 kV and equipped with a CCD camera (Mega-view SIS). The point resolution of the TEM used is 0.24 nm. A double-tilt holder with tilt limits of $\alpha = \pm 45^\circ$ and $\beta = \pm 25^\circ$ was used for the present studies. TEM was performed in imaging, selected area diffraction (SAD) and convergent beam electron diffraction (CBED) modes. The selected area (SA) aperture used in the present investigation was of 10 μm diameter, which could select ~140 nm diameter circular region on the sample. The SAD and CBED patterns were taken by tilting the required zone exactly along the beam direction. This was done partially by the double-tilt holder and finally using the beam-tilt facility in the dark-field mode. The CBED patterns have been taken in the wide-angle mode. All the TEM photographs, particularly SAD and CBED patterns, which have been presented here are properly enhanced for clear visibility of even the weakest details like weak superlattice spots and the HOLZ rings. In as-exposed diffraction patterns, these features remain undetected otherwise. During TEM analysis, energy dispersive X-ray spectrometry (EDXS) was also carried out in various domains of different grains. The measured composition was found to match with the intended ones within the typical error (~1%) of the EDXS analysis.

3. Results and discussion

Fig. 1 shows the powder XRD pattern of the SCT40 ceramics. It was Rietveld refined using *Pbcm* space-group with a goodness of fit of 2.48. Absence of any unaccounted peak shows the formation of impurity-free ceramics. The superlattice peaks arising due to the antiferroelectric ordering are indicated as AFE in Fig. 1. An enlarged view of the superlattice peaks is shown in the corresponding inset. Identifying the coexistence of structurally close phases, which differ only in the presence (or absence) of some very weak reflections, is usually not possible by lab XRD data. Therefore, extensive TEM investigation was carried out on various thin regions of the ion-polished sample of SCT40. These grains were found to be divided into various domains. Each domain of a grain was thoroughly analyzed using SAD and wide-angle CBED. TEM investigations at an elevated temperature of 100 °C were also carried out to observe the structural and microstructural changes occurring during antiferroelectric to paraelectric phase transition and vise versa. Details of the results obtained and its interpretation are presented in the following.

3.1. Occurrence of superlattice reflections: Evidence of cell doubling of antiferroelectric phase

Fig. 2 depicts a typical electron micrograph of SCT40 taken at RT along [100]-type zone of the perovskite lattice. It can be seen that a single grain is divided into various domains. The domains have been marked for the clarity of its identification. From these domains SAD and CBED patterns were taken after orienting them along the exact zone axes. Fig. 3 presents (a) SAD and (b) CBED patterns taken from the domain marked D2 and (c) SAD and (d) CBED patterns from the domain D7. The diffraction spots of the two SAD patterns have been properly indexed and the directions have also been marked. Fig. 3a is a typical ZOLZ pattern seen along the major axis [001] of the *Pbnm*

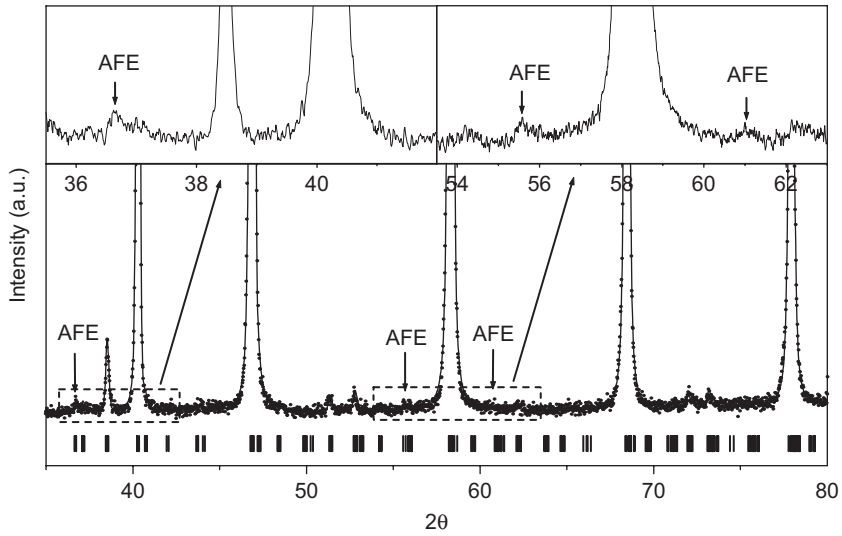

Fig. 1. Rietveld-refined room temperature XRD data of SCT40 ceramic with the *Pbcm* structure. Insets show the enlarged view of the superlattice peaks corresponding to antiferroelectric ordering.

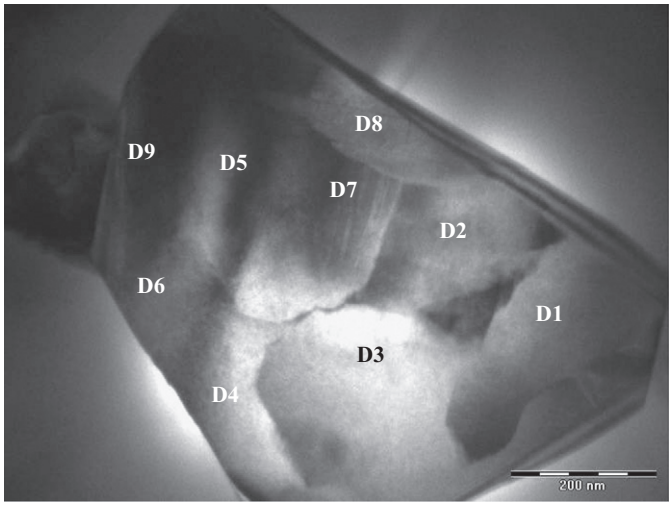

Fig. 2. Electron micrograph exhibiting the antiferroelectric domains with the *Pbcm* structure. Domain contrast appears due to 90° rotation domains. The domains marked by D3 and D8 are of the *Pbnm* phase.

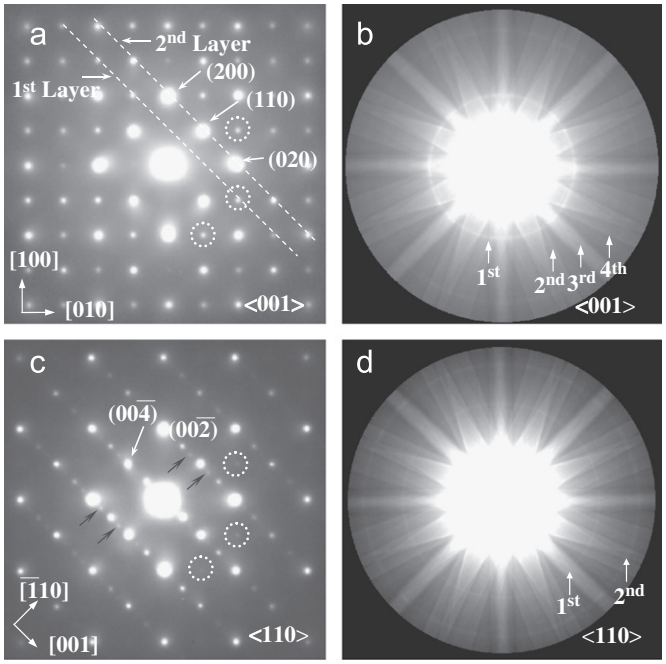

Fig. 3. Selected area diffraction (SAD) and convergent beam electron diffraction (CBED) patterns taken along (a,b) [001] and (c,d) [110] zones of the *Pbcm* phase from domains D2 and D7 respectively. The occurrence of the FOLZ ring as well as the superlattice spots as indicated by arrows exhibit the cell doubling corresponding to 15.5 Å.

and Pbcm. It should be noted that the spots with indices $\{h00\}$ and $\{0k0\}$ with h and k odd are forbidden in both *Pbnm* and *Pbcm* but are appearing as a result of double diffraction [6]. The FOLZ ring, as marked by 1st in the CBED pattern of Fig. 3a, measures 15.5 Å periodicity in the direct space and hence corresponds to the [001] reciprocal layer of the *Pbcm* phase. This is double the c-parameter (7.78 Å) of the *Pbnm* phase. It should be noted that the cell doubling occurs during paraelectric (*Pbnm*) to antiferroelectric (*Pbcm*) phase transition at ~355 K [14,15]. The other HOLZ rings as indicated by arrows are relatively weak. The direct evidence of cell doubling along the [001] direction can be found in the SAD pattern shown in Fig. 3c taken from domain D7 along [110], and the corresponding direct lattice-resolution micrograph as shown in Fig. 4. The presence of extra spots in the middle of the fundamental spots due to the *Pbnm* phase (as indicated by arrows in Fig. 3c) and the corresponding 15.5 Å lattice fringes in Fig. 4 approve the cell doubling of the antiferroelectric phase. The HOLZ rings in the [110]-zone CBED are marked as 1st and the 2nd in Fig. 3d. These rings appear as a result of intersection of the Ewald sphere with the reciprocal lattice layers indicated as 1st layer and 2nd layer in the ZOLZ given in Fig. 3a. Here we would like to

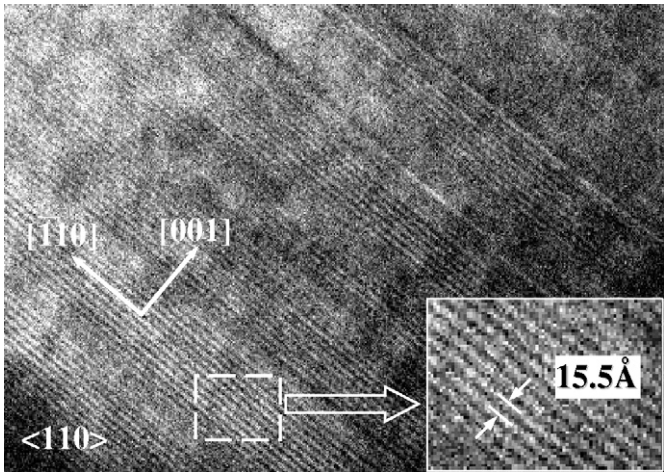

Fig. 4. Electron micrograph showing the 15.5 Å lattice fringes corresponding to cell doubling along the *c*-axis of the *Pbnm* phase.

emphasize that the CBEDs taken along the [001] zone of the *Pbnm* and along the [110] zone of both *Pbcm* and *Pbnm*, would overall appear identical and the diameters of FOLZ and SOLZ rings corresponding to both the phases would match. This can be realized by comparing the two CBEDs in Fig. 5b and d. The [001]- and [110]-type zones of *Pbcm* and *Pbnm* actually correspond to the $\langle 100 \rangle$-type zones of the basic perovskite structure. The SOLZs in the CBEDs taken along the [001] and [110] zones of *Pbnm* appear due to the basic [001]-type reciprocal lattice layers of the perovskite structure itself. The FOLZs in the [001]- and [110]-zone CBEDs correspond to the reciprocal lattice layers arising exactly in the middle due to the distortion-induced ordering in the basic perovskite structure. For [110]-zone CBED, the reciprocal lattice layers giving rise to the 1st and the 2nd rings will be directly seen in the [001]-zone SAD (ZOLZ) pattern. These are marked as 1st and 2nd layers in Fig. 3a.

The superlattice reflections appear as a result of doubling of the *c*-parameter of the paraelectric (*Pbnm*) phase. This has been attributed to the effect of antiparallel displacement of Ti^{4+} and Sr^{2+}/Ca^{2+} ions within the orthorhombic cell of the paraelectric phase. Such antiferroelectric phase transition was first observed in $NaNbO_3$ [17] and later identified for SCT by Ranjan et al. [10]. Extensive XRD studies on SCT have been carried out by Ranjan et al. [11] and Mishra et al. [14,15].

In Fig. 3c, besides the weak spots occurring due to superlattice ordering along the [001] direction, few extra weak spots in the center of the main square net of the perovskites reflection can also be seen. Few of them have been circled in Fig. 3c. These spots have nothing to do with domain D7. They come from the boundary of the neighboring domain D2. It can be noted that domain D7 is smaller than 140 nm, which the smallest available SA aperture covers, and therefore it was not possible to avoid the contributions coming from the boundaries of the neighboring domain D2. The reflections from domain D2,

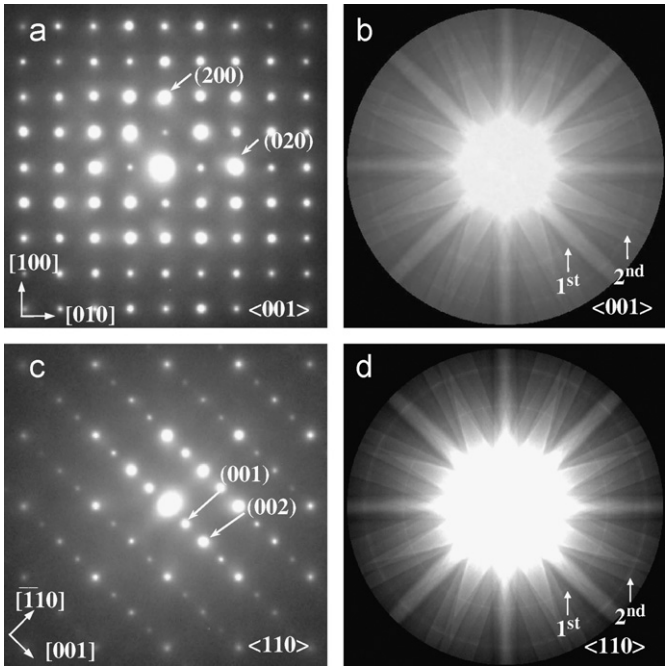

Fig. 5. SAD and CBED patterns taken along (a, b) [001] and (c,d) [110] zones respectively from domains D3 and D8 of the *Pbnm* phase. The absence of the FOLZ ring in the [001]-zone CBED and superlattice spots in [110]-zone SAD pattern approve the presence of the *Pbnm* phase at RT in SCT40.

which contribute to the circled spots in Fig. 3c, are also marked (circled) in the SAD as shown in Fig. 3a.

3.2. Coexistence of paraelectric (*Pbnm*) and antiferroelectric (*Pbcm*) phases

The antiferroelectric phase-transition observed for SCT40 is of the first order [10,15]. It is known that for a first-order phase transition, coexistence of high- and low-temperature phases is expected to occur over a range of temperatures around the transition temperature [16]. Since in the present case the transition temperature is not too far above the room temperature, there is a finite chance of observing the coexistence of *Pbnm* and *Pbcm* phases at room temperature itself [15]. As expected, we did find the electron diffraction evidence of the coexistence of *Pbnm* and *Pbcm* phases in SCT40.

Nearly all the domains, examined in different grains, show SAD and CBED patterns corresponding to the *Pbcm* phase only. But there were few domains like D3 and D8, which exhibited characteristically different SAD and CBED patterns. Fig. 5 presents the [001]-zone (a) SAD and (b) CBED patterns from domain D3 and the [110]-zone (c) SAD and (d) CBED patterns from domain D8. The SAD pattern in Fig. 5a looks qualitatively similar to that of in Fig. 3a but the diffraction features in the CBEDs are completely different. Unlike in Fig. 3b, the CBED in Fig. 5b does not contain the FOLZ ring corresponding to 15.5 Å. Rather it contains FOLZ corresponding to 7.78 Å, which belongs to the period along [001] of the *Pbnm* phase.

Similarly, unlike the SAD pattern shown in Fig. 3c, complete absence of the superlattice spots can be seen in the [110]-zone pattern in Fig. 5c. This approves that the domains D3 and D8 belong to the *Pbnm* phase only. Here it should be mentioned that the coexistence of *Pbnm* and *Pbcm* phases was not observed in every grain. Only few grains could show such features. A rough estimate of the abundance of the coexisting phases as examined through SAD and CBED on various domains spread over various grains would no way exceed ~5%. Thus at RT the majority of the SCT40 ceramic is an antiferroelectric (*Pbcm*) phase, coexisting with a minor fraction of the paraelectric (*Pbnm*) phase. We very thoroughly examined the compositions of the domains exhibiting the *Pbnm* phase and the nearby domain exhibiting the *Pbcm* phase. As already mentioned, we could not observe any significant composition difference above the typical error (~1%) of the EDXS analysis.

In the absence of any appreciable composition difference, the observed coexistence of paraelectric (*Pbnm*) and antiferroelectric (*Pbcm*) phases at RT, ~55 K lower than the transition temperature for the majority of the bulk, suggest that the observed coexistence is intrinsic to the nature of first-order phase transition from paraelectric to antiferroelectric [15]. Before we proceed to discuss the actual source of broadening of the transition, keeping in view the transition temperature of 355 K, which is close to RT, we would like to scrutinize the effects of possible artifacts arising due to electron beam heating. At 200 kV an electron beam may cause appreciable local temperature rise if deliberately converged (~100 nm) on the sample. But in the imaging mode the electron beam is very much divergent and therefore heating is not at all appreciable. This is approved by our earlier TEM experimentation on charge-ordered manganites carried using the same machine and similar beam condition, where we could perform temperature-dependent diffraction measurements and reproduce the charge-ordering temperature obtained through resistivity measurement [18]. Had the electron beam heating been really effective, the superlattice spots in Fig. 3c and the 1st ring in the CBED in Fig. 3b would have never been seen in any of the domains or it would have appeared and disappeared while beam divergence was varied. But no such thing was observed. The domains showing *Pbnm* and those showing *Pbcm* both were found to be invariant during the TEM analysis at RT. This clearly depicts that the observed coexistence is not at all an artifact of electron beam heating of the sample. It is well known that the presence of disorder including strain and point defects may broaden the first-order phase transition, i.e. one may observe a high-temperature phase below the super cooling point and a low-temperature phase above the super heating point. In the present case the source of strain may be two-fold. Firstly the inter-grain strain at the grain boundaries might result due to anisotropic lattice parameter change during solid–solid phase transformation from *Pm3m* to *Pbnm* at ~530 °C [19] while being furnace cooled after the sintering process. Since the grain boundaries are already glued much above 530 °C, the resulting anisotropy will produce strain. The other source of strain may be the point defects present in the sample. The recently discussed [20] symmetry conforming the short-range order (SC-SRO) property of the point defects has been reported to cause unusual macroscopic changes in the physical properties of bulk that undergo diffusionless (matensitic) transformation, for example the occurrence of rubber-like elastic properties in alloys [21] and large reversible electro-strain in ferroelectrics [22]. Creation of a point defect, which may be substitutional, vacancies, impurities etc., slowly acquire the symmetry properties of the surrounding atomic arrangement of the matrix phase. Now if a martensitic transformation takes place, the symmetry of the atomic arrangement around the defect changes but the SC-SRO of the defects remains the same because the transformation is diffusionless. For changing the SC-SRO of the defects, diffusion of the atomic species is required, which may take very long time; it may range from a few hours to a few 100 s of hours depending on the temperature. Now the presence of defects with SRO, not conforming to the long-range order symmetry of the phase, causes internal strain, which may slightly deform the symmetry of the transformed phase [20] and even cause macroscopic flip of the ferroelectric domains giving rise to the large reversible electro-strain in $BaTiO_3$ [22]. In a systematic aging experiment these SC-SRO of defects has been found to shift the transition temperature in $BaTiO_3$ [23]. In the present perovskite SCT also the transformation is diffusionless. For SCT40, the final sintering took place at 1300 °C for 24 h. Therefore the defects conforming to the *Pm3m* will stabilize. The *Pm3m* to *Pbnm* transformation occurs at ~530 °C, and *Pbnm* to *Pbcm* at ~80 °C. The sample cools from 530 °C to RT only within few hours. Since aging at 530 °C is not sufficient not all defects will conform to the *Pbnm* and most of the defects will still conform to the *Pm3m* symmetry and will cause internal strain opposing the antiparallel displacement mode of cations in some domains where its density is significant. This may inhibit the transformation of *Pbnm* to *Pbcm* in some domains.

3.3. High-temperature TEM studies of SCT40

We also investigated the antiferroelectric (*Pbcm*) to paraelectric (*Pbnm*) phase transformation at high temperatures using the double-tilt holder with the facility to heat the sample up to 100 °C (~373 K). We heated the same SCT40 sample to ~100 °C, across the transition temperature, and examined the domains D2 and D7, Fig. 2, exhibiting the antiferroelectric (*Pbcm*) phase at RT. Fig. 6a and c represent the (a) [001] and (c) [110] SAD patterns taken from the same domains D2 and D7 at ~100 °C, from which the SADs shown in Fig. 3a and c were taken. As compared to the [110]-zone SAD in Fig. 3c and [001]-zone CBED in Fig. 3b taken at RT, the complete absence of the superlattice spots in Fig. 6c and the 1st HOLZ ring

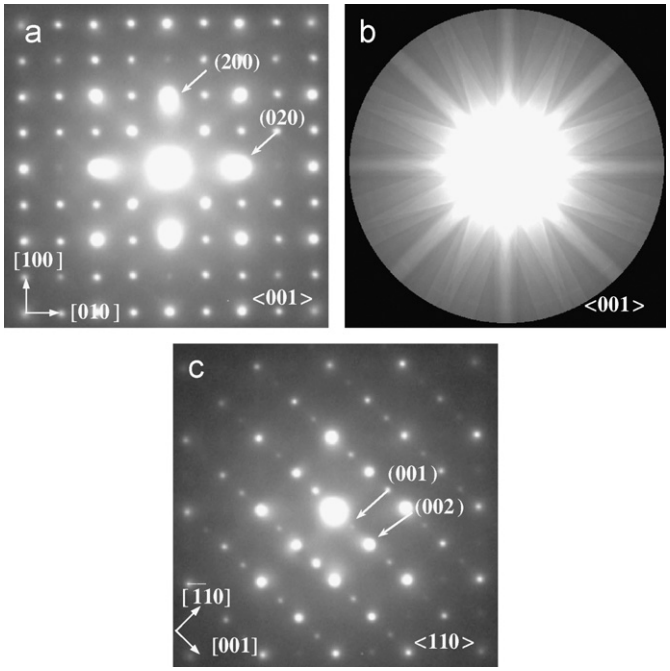

Fig. 6. SAD and CBED patterns taken at 100 °C along the (a,b) [001] of domain D2 and (c) [110] zones of domain D7, which show the *Pbcm* phase at RT. The absence of the 15.5 Å FOLZ ring in [001]-zone CBED and the superlattice spots in [110]-zone SAD pattern show that the *Pbcm* has transformed to the *Pbnm* phase.

corresponding to 15.5 Å periodicity corresponding to [001]-zone CBED in Fig. 6b can be seen. The absence shows that these patterns correspond to the *Pbnm* phase at 100 °C. Since the scattering vectors corresponding to the HOLZs are usually much larger, the thermal effects may affect them to a greater extent. Therefore it appears to be necessary to discuss the direct effect of heating on the intensities of the HOLZ rings. Heating would increase the lattice vibration leading to decrease in the Debye–Waller factor. Decreased Debye–Waller factor decreases the intensities of diffraction peaks. The Debye–Waller factor is given as $\exp(-2M)$, $M = Cu^2g^2$, where C is a constant, u is the mean square amplitude of the lattice vibration at a temperature and g is the diffraction vector corresponding to the peak (HOLZ ring). Since the diffraction vector corresponding to the 4th HOLZ ring will be twice the diffraction vector corresponding to the 1st HOLZ ring, the Debye–Waller factor will always be lower for the 4th HOLZ ring as compared to the 1st HOLZ ring i.e. the 4th HOLZ ring will suffer more fractional decrease of intensity due to thermal effect than the 1st HOLZ ring. As can be seen in Fig. 3b the 4th HOLZ ring is much weaker than the 1st HOLZ ring. If the thermal vibration is at all severe, the 4th HOLZ's intensity should vanish before the 1st HOLZ's one. But the observed fact is contrary. The 1st HOLZ ring, which is much more intense as compared to the 4th HOLZ ring completely vanishes and the relatively weaker 4th HOLZ ring is still well defined and visible. This clearly indicates that the disappearance of the 1st HOLZ ring is purely structural in origin. At temperatures above 355K the antiferroelectric (*Pbcm*) phase undergoes paraelectric (*Pbnm*) phase transition in which cell-doubling ordering along [001] vanishes and hence the corresponding 1st and 3rd HOLZ rings also vanish. Here it should be mentioned that the 2nd HOLZ ring in Fig. 3b should be present even after *Pbcm* to *Pbnm* phase transformation but this has almost merged into the background at 100 °C. This is purely due to the decreased Debye–Waller factor at high temperature. Fig. 3b shows that at RT itself the intensity of the 2nd HOLZ ring is much weaker than the 4th HOLZ's intensity, hence unlike the 4th HOLZ it did not survive the thermal vibration effect and effectively merged into the background.

The antiferroelectric (*Pbcm*) to paraelectric (*Pbnm*) phase transition is obvious not only in the electron diffraction data but also in the corresponding electron micrographs. The electron micrographs taken at high temperature contain information of different nature. We could recycle the sample temperature between RT and 100 °C and record the electron micrographs at 100 °C after every heating, and at room temperature after every cooling. Fig. 7 shows the TEM micrographs of a single grain of SCT40. These are recorded at different stages of heating and cooling cycles. The starting RT micrograph, Fig. 7a, and the RT micrograph recorded after the completion of the first heating–cooling cycle across the transition temperature, shown in Fig. 7c, possess completely different domain structures. The entity of the selected single grain can only be identified by the presence of some intrinsic markers like the dislocations, indicated by arrows. But the high-temperature (100 °C) micrographs, Fig. 7b and d, which are completely different from the corresponding RT ones, were found to be the same after each heating–cooling cycles.

The observed reshuffling of the RT domain structure after every thermal cycle is due to the random selection of the nucleation sites for the antiferro distortion for the growth of antiferroelectric (*Pbcm*) domains on the commencement of phase transformation during cooling. The 100 °C micrographs have the same domain structure but a comparison between Fig. 7a and b clearly shows that the domain structures of *Pbcm* and *Pbnm* phases are completely different. The high-temperature domain configuration has been defined during the phase transformation at 530 °C while the SCT40 ceramic pellet was being cooled after its final sintering at 1300 °C. The high-temperature phase of SCT40 perovskites is *Pm3m*, which transforms to orthorhombic after being cooled across 530 °C [18]. Since the domain structure observed at 100 °C has been defined during cubic (*Pm3m*) to orthorhombic (*Pbnm*) phase transformation occurring at ~530 °C, much higher than 100 °C, it will change only when we cycle it through 530 °C. Any thermal cycle lower than that will not change the observed domain structure at 100 °C. The domain contrast observed in the 100 °C micrograph arises due to 90° rotational twin-domains of the *Pbnm* phase imaged along

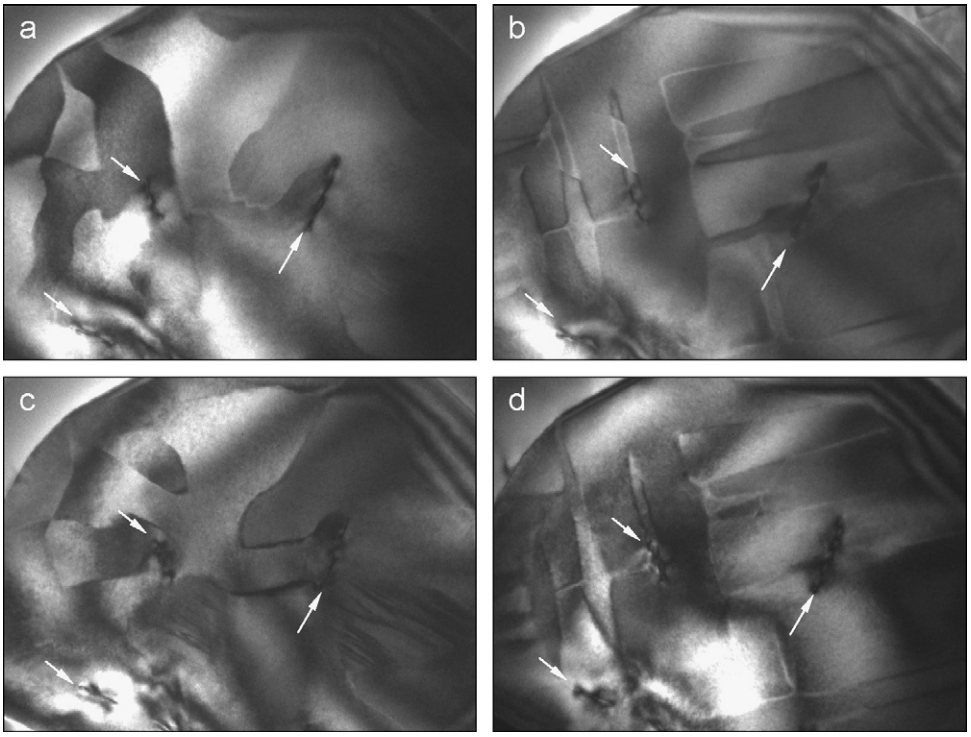

Fig. 7. Electron micrographs taken in different situations of the same grain, (a) starting RT, (b) at 100 °C during the 1st heating, (c) at RT after first cooling from 100 °C and (d) again at 100 °C during the 2nd heating. The invariance of the domain structure in the micrographs taken at 100 °C and the thermal cycle dependence of the domain structure in RT micrographs can be clearly noticed. Drastic change in the domain configuration during *Pbnm* to *Pbcm* transformation clearly indicates that antiferrodistortive transition taking place during the transition is of different origin and it has nothing to do with the tilt scheme present prior to the transition.

the [001] orientation. From the RT micrographs it is clear that during *Pbnm* to *Pbcm* transformation the domain boundary definition has completely changed. It appears that the antiparallel displacements of Ti^{4+} and Sr^{2+}/Ca^{2+} ions within the orthorhombic cell of the paraelectric phase do not follow the predefined $a^-a^-c^+$ tilt scheme. Otherwise we could have observed the *Pbcm* domains following the hierarchy of the existing *Pbnm* domain structure. It has been described in [11,17] that in the *Pbcm* phase the doubling along the *c*-axis involves four perovskite blocks. The upper two 1 and 2, and the lower two 3 and 4 are linked with the $a^-a^-c^+$ tilt scheme, but 2 and 3 are linked with the $a^-a^-c^-$ tilt scheme. This effectively means as completely new tilt scheme. What is remarkable is that during transformation this new tilt scheme is independently operated irrespective of the prior tilt scheme $a^-a^-c^+$. Therefore it erases all signatures of the *Pbnm* domain. The exact recovery of the *Pbnm* domain configuration at 100 °C, after every thermal cycle, indicates the presence of some memory mechanism, which retains the memory of the "domain structure" defined above the antiferroelectric to paraelectric phase transition. The observed microstructural memory effect is similar to that of reported for the Au–Cd alloy [20]. Such memory effect arises due to the strain produced by the SC-SRO property of the point defects present in the parent phase. During diffusionless transformation from *Pbnm to Pbcm* the defects, which have already stabilized and conformed to *Pbnm* symmetry, will remain in the same state of conformation even in the *Pbcm* as well. The strain produced by these defects may act as a guideline for reproducing the domain structure in the *Pbnm* phase.

4. Conclusions

Based on the above-described results and discussions of TEM studies carried out on SCT40, we conclude that we have presented the very first cleansing evidence of cell-doubling during paraelectric (*Pbnm*) to antiferroelectric (*Pbcm*) phase transition. We could observe the coexistence of the *Pbnm* and *Pbcm* phases as a result of strain-broadened first-order paraelectric (*Pbnm*) to antiferroelectric (*Pbcm*) phase transition. Keeping in view the completely uncorrelated domain structures across the *Pbnm* to *Pbcm* phase transition temperature, it is concluded that the antiparallel displacements of Ti^{4+} and Sr^{2+}/Ca^{2+} ions within the orthorhombic cell of the antiferroelectric *Pbcm* phase do not follow the predefined $a^-a^-c^+$ tilt schemes present in the paraelectric *Pbnm* phase. But during the transformation, a new tilt scheme is independently operated, redefining a completely new domain structure and also allowing the antiparallel displacement of Ti^{4+} and Sr^{2+}/Ca^{2+} ions. The exact recovery of the *Pbnm* domain configuration at 100 °C after

each thermal cycle indicates the presence of some kind of "domain structure memory" effect, which appears to be a macroscopic manifestation of the symmetry conforming short-range order property of point defects present in the bulk.

Acknowledgments

The Authors gratefully acknowledge Dr. P. Chaddah, the Director, and Prof. Ajay Gupta, the Center Director of UGC-DAE CSR-Indore, for their encouragement and interest in the work. We acknowledge the fruitful discussions with Prof. Dhananjai Pandey SMST-BHU Varanasi. One of the authors, Shahid Anwar, also acknowledge CSIR-India for financial support as SRF.

References

[1] A.M. Glazer, Acta Crystallogr. B 28 (1972) 3384.
[2] A.M. Glazer, Acta Crystallogr. A 31 (1975) 756.
[3] D.I. Woodward, I.M. Reaney, Acta Crystallogr. B 61 (2005) 387.
[4] C.J. Ball, B.D. Begg, D.J. Cookson, G.J. Thorogood, E.R. Vance, J. Solid State Chem. 139 (1998) 238–247.
[5] C.J. Howard, R.L. Withers, Z. Zhang, K. Osaka, K. Kato, M. Takata, J. Phys.: Condens. Matter 17 (2001) L459.
[6] Anwar. Shahid, N.P. Lalla, J. Phys.: Condens. Matter 19 (2007) 436210.
[7] T. Yamanaka, N. Hirai, Y. Komatsu, Am. Mineral. 87 (2002) 1183.
[8] M.A. Carpenter, C.J. Howard, K.S. Knight, Z. Zhang, J. Phys.: Condens. Matter 18 (2006) 10725.
[9] J.G. Bednorz, K.A. Muller, Phys. Rev. Lett. 52 (1984) 2289.
[10] R. Ranjan, D. Pandey, N.P. Lalla, Phys. Rev. Lett. 84 (2000) 3726.
[11] R. Ranjan, D. Pandey, J. Phys.: Condens. Matter 13 (2001) 4239; R. Ranjan, D. Pandey, J. Phys.: Condens. Matter 13 (2001) 4251.
[12] S.K. Mishra, R. Ranjan, D. Pandey, Brendan. J. Kennedy, J. Appl. Phys. 91 (2002) 4447.
[13] R. Ranjan, D. Pandey, V. Siruguri, P.S.R. Krishna, S.K. Paranjpe, J. Phys.: Condens. Matter 11 (1999) 2233.
[14] S.K. Mishra, R. Ranjan, D. Pandey, H.T. Stokes, J. Phys.: Condens. Matter 18 (2006) 1885.
[15] S.K. Mishra, R. Ranjan, D. Pandey, P. Ranson, R. Ouillon, J.P. Lucarre, P. Pruzan, J. Phys.: Condens. Matter 18 (2006) 1899.
[16] P. Chaddah, Pramana: J. of Phy. 67 (2006) 113.
[17] A.C.S. Cowley, K. Lukaszewicz, H.D. Megaw, Acta Crystallogr. B 25 (1969) 851.
[18] P.R. Sagdeo, Shahid. Anwar, N.P. Lalla, Solid State Commun. 137 (2006) 158.
[19] M.A. Carpenter, C.J. Howard, K.S. Knight, Z. Zhang, J. Phys.: Condens. Matter 18 (2006) 10725.
[20] Xiaobing Ren, Kazuhiro Otsuka, Phy. Rev. Lett. 85 (2000) 1016.
[21] Xiaobing Ren, Kazuhiro Otsuka, Nature 389 (1997) 579.
[22] Xiaobing Ren, Nat. Mater. 3 (2004) 91.
[23] Dazhi Sun, Xiaobing Ren, Kazuhiro Otsuka, Appl. Phys. Lett. 87 (2005) 142903.